



Experimental and analytical investigations of the removal of spatters by various process gases during the powder bed fusion of metals using a laser beam

Siegfried Baehr¹ · Tobias Klecker¹ · Sebastian Pielmeier¹ · Thomas Ammann² · Michael F. Zaeh¹

Received: 12 January 2023 / Accepted: 5 August 2023 / Published online: 17 August 2023
© The Author(s) 2023

Abstract

The powder bed fusion of metals using a laser beam (PBF-LB/M) is increasingly being utilized in industrial applications. This is due to several advantages over conventional manufacturing processes when it comes to the fabrication of complex part designs. However, the process still poses various challenges that have to be overcome. One of these challenges is the formation of a significant amount of spatters and fumes. These could attenuate the laser beam or decrease the powder reusability. To lower their negative impact on the process and the mechanical properties of the parts, a process gas flow is used in PBF-LB/M to remove these by-products from the processing zone. This study was, therefore, dedicated to investigating the potential of various gases on the removal of spatters. The focus was placed on argon, helium, and their mixtures. After theoretical considerations determining the range of applicable gas flow velocities, the experimental results unveiled the real spread of spatters over the powder bed and their characteristics. Whilst the removal of spatters was found to be worse for an argon–helium gas mixture at comparable gas flow velocities, increasing the velocity turned out to be a proper measure to enhance the removal for low-density gases. At this flow condition, the use of the argon–helium gas mixture led to a similar removal of spatters and the creation of a lower spatter mass in total (reduced to 40%) compared to argon.

Keywords Additive manufacturing · Laser powder bed fusion · PBF-LB/M · Process by-products · Process gases

1 Introduction

The powder bed fusion of metals using a laser beam (PBF-LB/M) is an additive manufacturing process increasingly being used in industry. Compared to conventional

manufacturing technologies, major advantages of the PBF-LB/M process are, for example, the freedom in the part design and the localized use of material [1]. These advantages especially qualify the process for applications where complex integrated part designs can lead to significant improvements in the performance of the part. However, negative side effects of the process, such as the creation of by-products (fumes and spatters) due to a very high localized heat input, can lead to problems hindering its further use in the industry. The consequences of these side effects range from poor powder reusability to reduced part properties. The driving mechanisms of the creation and the possible influences of spatters on the process and the manufactured parts were investigated in various studies [2–6]. Chen et al. [2] found that the occurring metal vapor jet is the main driver of spattering in the PBF-LB/M process, which entrains liquid metal ejections from the melt pool as well as particles from the surrounding area. The spatters can then settle in the powder bed and form agglomerates with the powder particles, which can reduce its reusability [3]. These findings were confirmed and extended by a review study by Li et al. [4].

✉ Siegfried Baehr
siegfried.baehr@iwb.tum.de

Tobias Klecker
tobias.klecker@tum.de

Sebastian Pielmeier
sebastian.pielmeier@tum.de

Thomas Ammann
thomas.ammann@linde.com

Michael F. Zaeh
michael.zaeh@iwb.tum.de

¹ TUM School of Engineering and Design, Institute for Machine Tools and Industrial Management, Technical University of Munich, 85748 Garching, Germany

² Linde GmbH, 85716 Unterschleissheim, Germany

With regard to the part properties, unmolten and residual spatters can lead to lack of fusion pores in the parts and, thus, reduce their performance [4]. Additionally, they can interact with the laser beam and interrupt the energy input [4–6].

A novel strategy for lowering the spatter formation based on multi-laser illumination realized via diffractive optical elements was presented by Slodczyk et al. [7]. They demonstrated an increased productivity whilst keeping the number of spatters constant. This was attributed to a more homogeneous temperature distribution due to a more stable melt pool. However, in today's standard PBF-LB/M processes, other measures have to be identified and qualified to lower the spattering and increase the process stability. This can be achieved by varying the primary process parameters at the cost of low productivity, for example by lowering the scan speed [7]. In this context, the process gas flow was found to be another parameter that can influence the formation and removal of spatters whilst maintaining the process speed. Before the process, the build chamber is flooded with an inert gas, thus avoiding interactions between the liquid metal and the ambient atmosphere (e.g., oxidation). During the process, a constant gas flow is guided over the build platform to remove fumes and spatters. Studies on the influence of the gas flow highlighted the general importance of the gas flow towards the implementation of a stable process [6, 8]. Ladewig et al. [6] applied a maximum flow rate of 65 m³/h and concluded that the highest possible gas flow velocity needs to be applied to guarantee a proper removal of process by-products. However, no differentiation was made towards the gas type and no recommendations were given on the settings for a proper spatter removal.

Various studies on the interactions between the gas flow and the spatters have been conducted, applying different observation and sampling techniques: high-speed imaging [9–11], Schlieren imaging and shadowgraphy [12–14], high-speed stereovision [15], or X-ray monitoring [16, 17]. These monitoring techniques offer limited information about the final settling of spatters in the powder bed and can only monitor spatters in flight. On the contrary, few studies have used in-situ powder sampling approaches to study the spread of spatters [18, 19]. Anwar et al. [18] found that spatters occur in different shapes and sizes. Larger spatters (diameter ~ 150 μm) tend to settle closer to the process zone compared to smaller spatters (diameter ~ 90 μm). These size classes for spatters have also been reported in other studies [20, 21]. However, when increasing the gas flow velocity, larger particles could effectively be dragged further away from the process zone. Regarding the shape of spatters, various types were reported depending on their forming mechanism and features [4, 16, 19, 21]. Spherical spatters are formed if there is sufficient time for solidification in flight, whilst agglomerated spatters occur as a consequence of a collision with another spatter or powder particle. Regarding the spatial spread of spatters over the powder bed, Anwar et al. [18] have reported mainly a spread along the scan direction.

Various studies have been conducted to investigate the influence of the gas type on the process and the manufactured parts [12–14, 22–25]. Besides the gases argon and nitrogen, which are currently mainly used in industry, the application of helium has been extensively studied. Due to its significantly different thermophysical properties (e.g., density, thermal conductivity), it has the potential to impact the PBF-LB/M process. A major finding of these studies is the higher cooling ability of helium compared to argon leading to less incandescent spatter and to

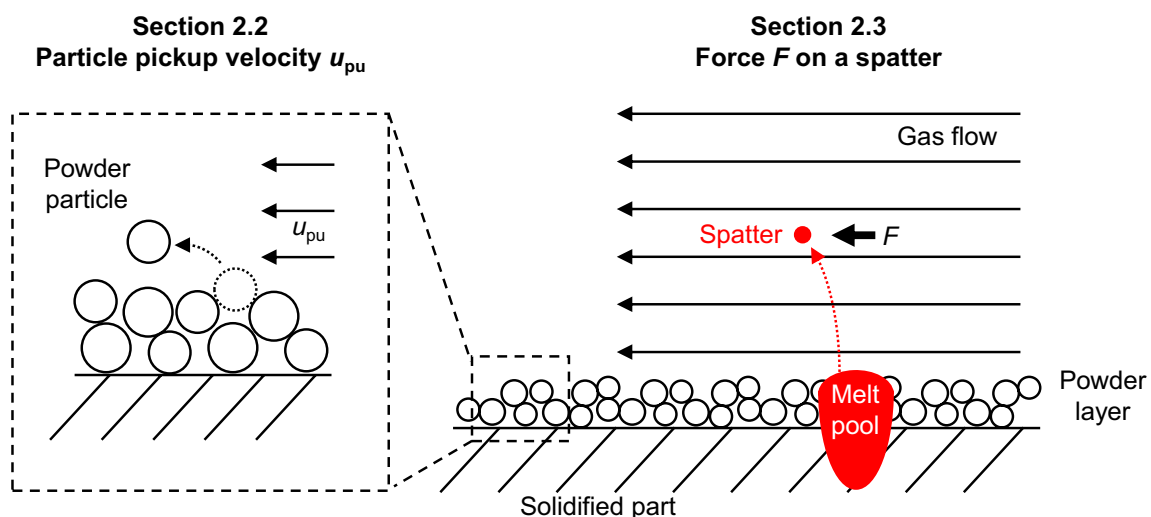


Fig. 1 Schematic representation of the theoretical considerations; u_{pu} : particle pickup velocity, F : force applied to a spatter particle by the gas flow

Fig. 2 Density ρ_g and dynamic viscosity η_g of argon (Ar), helium (He), and their mixture 70 vol% Ar + 30 vol% He (ArHe30) at norm conditions ($p = 1$ bar, $T = 25$ °C)

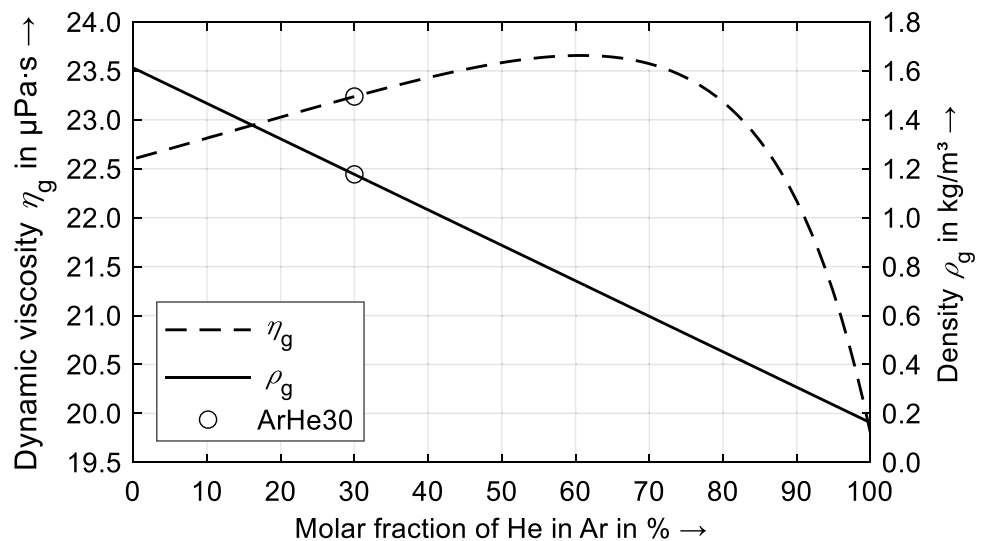


Table 1 Relevant physical quantities of argon (Ar), helium (He), and ArHe30 at norm conditions ($p = 1$ bar, $T = 25$ °C) [28]

	Gas density ρ_g in kg/m^3	Dynamic viscosity η_g in Pa s
Ar	1.612	22.6×10^{-6}
ArHe30	1.177	23.2×10^{-6}
He	0.162	19.8×10^{-6}

less metal vapor [12–14]. This can increase the process stability, as the laser attenuation is reduced and a more homogeneous energy input is provided. These findings were valid for various materials, which highlights the material-independent advantages of using helium in the PBF-LB/M process. Amano et al. [24] additionally found positive effects of helium on the microstructure when processing Ti-6Al-4V. In their study, the microstructure under helium was found to be finer and mainly composed of α' martensite resulting in enhanced mechanical properties. On the contrary, Stokes et al. [25] found that the velocity of spatters leaving the melt pool is significantly higher under helium than under argon due to its lower molecular mass. This could potentially lead to more spatters entering the laser path and, thus, needs to be avoided.

The state of research presented here shows that there have been extensive studies on the influence of the process gas on the by-products. Spatters have been classified in terms of size and shape. Various gas types were studied concerning their influence on the creation and removal of spatters. However, there is still a lack of confidence about the applicable ranges of gas flow velocities for various gases and the

resulting real spread of spatters over the powder bed during PBF-LB/M.

Therefore, this study aimed to analytically and experimentally investigate the interdependencies between the gas flow and the spatter removal using argon, helium, and their mixtures. First, analytical considerations are presented to determine the appropriate range of gas flow velocities. Subsequently, the ability of various gases to remove spatters is studied based on calculations of the drag force. These analytical considerations are compared to experimental results of spatter removal using a unique in-situ spatter collection device.

2 Theoretical considerations of the spatter removal

In this section, the influence of the various process gases on the powder bed and the removal of spatters is evaluated. As the density and the dynamic viscosity of the gas highly influence the occurring effects, the resulting physical properties of argon (Ar), helium (He), and their mixtures are described at the beginning. A two-step approach was used to analytically assess the relevant process phenomena. First, the maximum gas flow velocity per gas was calculated based on the particle pickup velocity u_{pu} . This is the velocity above which the first powder particles from the powder bed starts to be blown away. Second, the drag force that the gas flow exerts on a single spatter was calculated considering u_{pu} and used to compare the performance of various process gases. The two different areas of consideration are schematically summarized in Fig. 1. For all calculations, the physical quantities of the powder material and the pure gases provided in Sect. 2.1 were used. Throughout this study, the index “p”, the index “g”, and the index “s” represent

the powder properties, the gas properties, and the spatter properties, respectively.

2.1 Physical properties of argon, helium, and their mixtures

The density ρ_g of a gas mixture can be calculated via the density ρ_i and the molar fraction x_i of a number of n contributing gases with the assumption of ideal gases according to

$$\rho_g = \sum_{i=1}^n \rho_i \times x_i. \tag{1}$$

The dynamic viscosity η_g of a binary gas mixture ($n=2$) depends on the characteristic lengths of the contributing gases i and j and is, thus, a function of their molar masses M . It can be calculated according to Wilke [26] by

$$\eta_g = \sum_{i,j=1}^n \frac{x_i \times \eta_i}{\sum_j x_j \times Z_{ij}} \tag{2}$$

with

$$Z_{ij} = \frac{\left[1 + (\eta_i/\eta_j)^{1/2} \times (M_j/M_i)^{1/4}\right]^2}{\sqrt{8 \times (1 + (M_i/M_j))}}. \tag{3}$$

Figure 2 shows ρ_g and η_g of Ar, He and their mixtures depending on the molar fraction of He in Ar. The properties of 70 vol% Ar + 30 vol% He are highlighted individually, as this mixture is of particular relevance for the presented study.

As can be seen in Fig. 2, η_g reaches a maximum at around 60 vol% He in Ar. The density linearly decreases from Ar to He. Experimental evidence for the behavior of η_g in Ar–He gas mixtures can be found in the literature [27]. Table 1 summarizes the relevant gas properties used for the model calculations following the above-mentioned equations for Ar, He, and 70 vol% Ar + 30 vol% He. To enhance readability, this Ar–He mixture is referred to as “ArHe30” in this article.

2.2 Determination of possible gas flow velocities

In the PBF-LB/M process, the highest possible gas flow velocity needs to be achieved to ensure sufficient removal of process by-products [6]. To estimate the potential for the removal of process by-products of various process gases, the particle pickup velocity u_{pu} can be utilized. Kalman et al. [29] proposed an empirical model for the calculation of u_{pu} based on the dimensionless particle Reynolds number Re_p and the Archimedes number Arch. Following this model, u_{pu} depends on both the gas and

Table 2 Particle size distribution of the 316 L stainless steel powder used in this study

d_{10} in μm	d_{50} in μm	d_{90} in μm
28.0	41.2	56.6

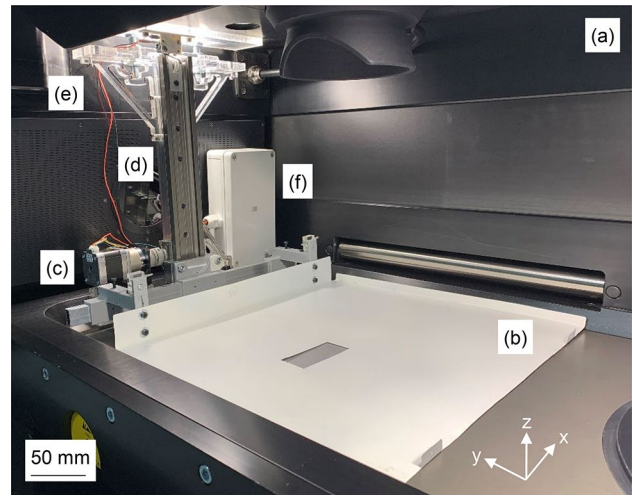


Fig. 3 Experimental setup for an in-situ collection of spatters: **a** Trumf TruPrint 3000 process chamber, **b** build platform cover, **c** electric stepper motor, **d** rope pull mechanism, **e** clamping mechanism, **f** sealed box for electronics; x : gas flow, y : recoating, z : build up

powder bed properties, and can be calculated for varying particle diameters d_p with the modification factor K_D for the flow profile (set to 50 mm in this study) by

$$u_{pu} = \frac{Re_p \times \eta_g}{d_p \times \rho_g \times K_D}. \tag{4}$$

The dimensionless Re_p is calculated via the dimensionless Arch. These two numbers describe particle movements in a fluid and account for gravitational as well as drag forces [30]. The calculation of Re_p is divided into three zones, which leads to a stepwise function for u_{pu} according to

$$Re_p = \begin{cases} \text{(I)} & 5 \times Arch^{3/7} & \text{for } Arch \geq 16.5 \\ \text{(II)} & 16.7 & \text{for } 0.45 < Arch < 16.5 \\ \text{(III)} & 21.8 \times Arch^{1/3} & \text{for } Arch \leq 0.45 \end{cases}. \tag{5}$$

Arch can be calculated with the particle shape modification factor K_Φ (set to 0.9 in this study [29]) by

$$Arch = \frac{g \times \rho_g \times (\rho_p - \rho_g) \times d_p^3}{\eta_g^2 \times K_\Phi}. \tag{6}$$

Zone (I) is valid for large particles, where gravitational forces dominate. Zone (III) applies to very fine particles,

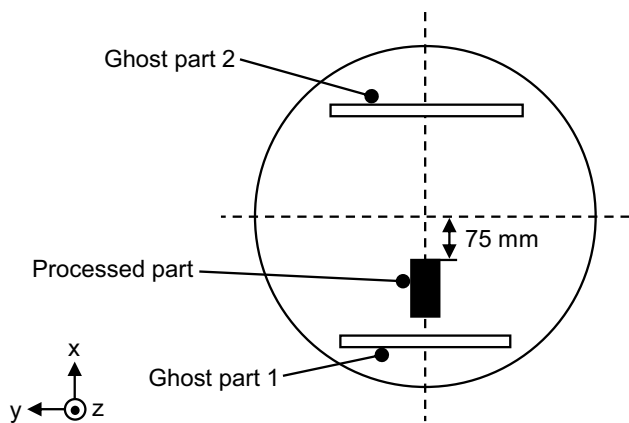


Fig. 4 Schematic build job layout

Table 3 Process parameters

Laser power in W	Scan speed in mm/s	Hatch distance in μm	Layer thickness in μm	Scan strategy
280	1000	100	60	Bidirectional

where mostly inter-particle forces have an effect on the particle cohesion. In zone (II), the ratios between cohesive and gravitational forces start to decrease with increasing d_p . Shen et al. [31] applied these calculations to powders for PBF-LB/M and defined suitable ranges for the gas flow velocity. Their experimental results using Ar as a process gas showed a good agreement with the model calculations for a variety of powder materials (e.g., 316L stainless steel). For further details on the model calculation, the reader is referred to [29] and [31].

2.3 Spatter removal by the process gas flow

To compare the ability of various gases to transport spatters away from the process zone, the force that a gas flow can apply to a spatter particle can be considered. In this study, the calculations of this force are subject to the following simplifications and limitations:

- Spatters are spherical.
- Spatters are initially at rest.

Considering these preconditions, the Stokes equation for the calculation of the drag force of a particle in a fluid flow can be utilized to compare various process gases. The resulting force F is determined with the drag coefficient c_w , the

spatter surface A_s , the spatter diameter d_s , and the gas flow velocity u_g by

$$F = \frac{1}{2} \times c_w \times \rho_g \times A_s \times u_g^2 = \frac{1}{2} \times c_w \times \rho_g \times \left(\left(\frac{d_s}{2} \right)^2 \times \pi \right) \times u_g^2. \tag{7}$$

Initially, a gas flow velocity of $u_g = 2$ m/s and a representative spatter diameter of $d_s = 100 \times 10^{-6}$ m were used. The drag coefficient c_w depends on the spatter Reynolds number Re_s . As the Stokes equation is only valid for $Re_s < 0.5$, where gravitational forces can be neglected, a correction factor must be applied for higher Re_s . This correction factor accounts for the increasing influence of the gravitational forces at increasing particle diameters. The drag coefficient c_w can be calculated stepwise by

$$c_w = \left\{ \begin{array}{ll} \frac{24}{Re_s} & \text{for } Re_s < 0.5 \\ \frac{24}{Re_s} \times (1 + 0.15 \times Re_s^{0.687}) & \text{for } 0.5 \leq Re_s < 1000 \end{array} \right\}, \tag{8}$$

with

$$Re_s = \frac{\rho_g \times u_g \times d_s}{\eta_g}. \tag{9}$$

This empirical model for the calculation of c_w has shown a high accuracy up to $Re_s = 1000$ [32].

In this study, an Ar process gas flow with a velocity of $u_g = 2$ m/s is considered as the reference condition. These conditions represent standard process conditions as they are commonly applied in research and industry [5, 33, 34]. To enhance the comparability, the calculated forces F per gas were normalized according to

$$\bar{F} = \frac{F}{F(Ar, u_g = 2\text{m/s})}, \tag{10}$$

with the force $F(Ar, u_g = 2$ m/s) that an Ar gas flow with a velocity of 2 m/s exerts on a spatter (reference conditions).

3 Materials and methods

3.1 Experimental setup

All experiments in this study were conducted on a Trumpf TruPrint 3000 PBF-LB/M machine. Its build platform had a diameter of 300 mm. The material was 316 L stainless steel powder (LPW, United Kingdom). The particle size distribution (PSD) of the powder samples was measured by optical analysis (Camsizer X2, Retsch, Germany) in size classes of 2 μm from 0 to 240 μm. The d_{10} , d_{50} , and d_{90} values of the virgin powder are shown in Table 2. Due to technical

Fig. 5 Optical analysis of the spatter distribution on the build platform cover (the laser processing zone is indicated with the black dotted box)

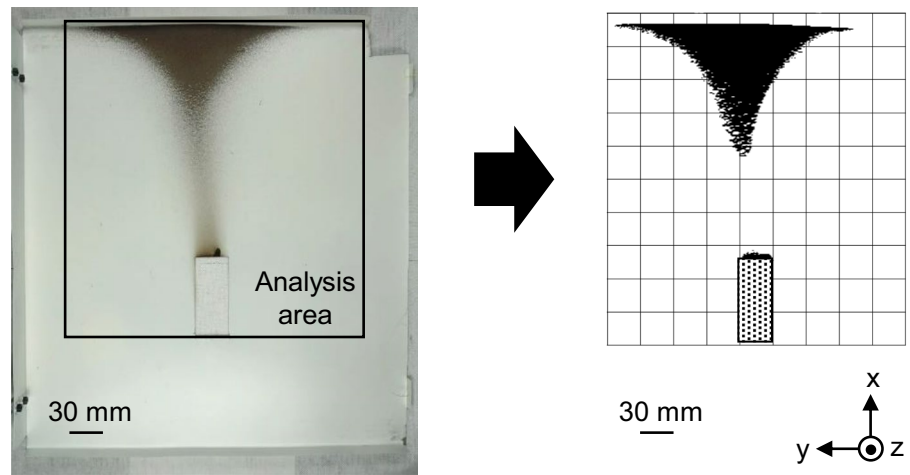
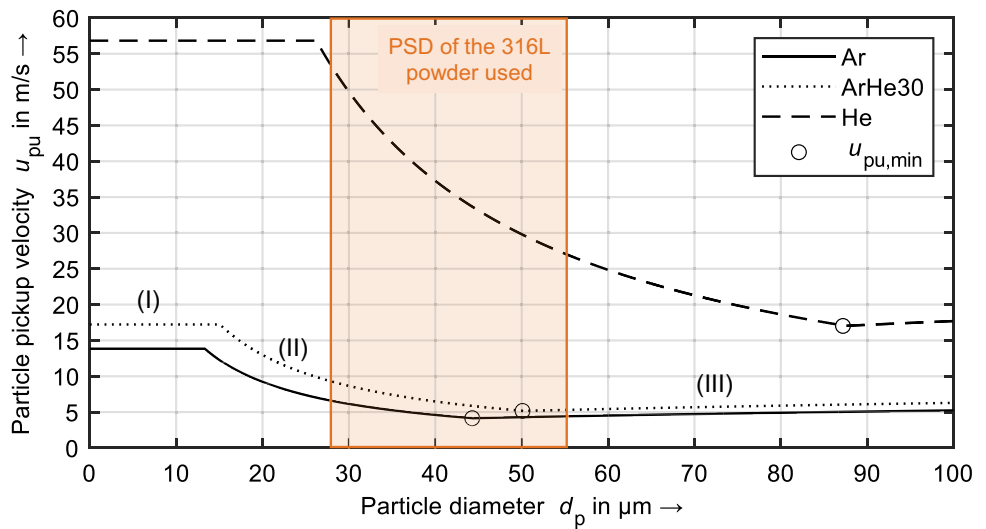


Fig. 6 Particle pickup velocities u_{pu} for three process gases depending on the particle diameter d_p ; different zones (I)–(III) for u_{pu} exemplarily shown for ArHe30



limitations of the PBF-LB/M machine used in the study, besides Ar, only ArHe30 could be used in the experiments.

To enable an in situ collection of spatters, a unique spatter collection device was built and implemented into the build chamber (see Fig. 3). Throughout this study, the x-direction indicates the gas flow direction, the y-direction is the recoating direction, and the z-direction represents the build direction. The main components of the device are a build platform cover with a thickness of 1 mm and a cutout for processing (b), an electric stepper motor (c), a rope pull mechanism (d), a clamping mechanism (e), and a sealed box containing the motor driver, an Arduino with Bluetooth control function, and the battery (f) (see Fig. 3). The device can be moved upwards and downwards. The build platform cover was spray painted in white colour to enhance the visibility of the spatters. Measurements of the surface roughness R_z were performed to ensure comparable flow conditions over the build platform cover. The surface roughness was determined to be $R_z = 41.66 \mu\text{m} \pm 18.47$, which lies in the range of the

Table 4 Minimum particle pickup velocities $u_{pu,min}$ with associated particle diameter d_p depending on the process gas

	$u_{pu,min} = u_{g,max}$ in m/s	d_p in μm
Ar	4.15	44.28
ArHe30	5.16	50.09
He	17.02	87.19

PSD of the powder used. Thus, comparable flow conditions were assumed in this study. During the PBF-LB/M process, the following procedure was performed:

1. The cover moves to the top end position (transition time = 15 s).
2. The recoater spreads a new layer of powder over the build platform.
3. The cover moves to the bottom end position where it lies flat on the build platform (transition time = 15 s).

4. The laser exposes the part.
5. The cycle starts with the first step again.

The build job layout is depicted in Fig. 4. It consisted of one solid block sized $50 \times 20 \times 5 \text{ mm}^3$, which was placed towards the front of the build platform according to Fig. 4. A bidirectional scan strategy was applied and oriented parallel to the x-direction. The experiments were conducted in a single execution. The process parameters were kept constant according to Table 3. Initial density measurements in cubes processed with these parameters revealed a mean relative density of $> 99.9\%$. To ensure comparable flow conditions in the experiments, gas flow velocity measurements using vane anemometry (TS26/16GE, Höntzsch, Germany) were conducted with both gases in advance. The setup and the results of these measurements are depicted in Appendix in Figs. 11 and 12, respectively.

To maintain a transition time for the movement of the cover and, thus, to avoid a collision with the recoater or an interaction with the laser beam, two additional parts were included in the build job layout. These “ghost parts”, which were $150 \times 5 \times 5 \text{ mm}^3$ in size, were processed with a laser power of 0 W, a scan speed of 1000 mm/s, a hatch distance of 0.1 mm and a layer thickness of 0.06 mm. This resulted in a time of 15 s per ghost part, during which the cover could move upwards or downwards. The ghost parts were placed in front of and behind the solid block (see Fig. 4).

3.2 Post-process analysis

Immediately after the experiments, the spatter distribution on the cover was analyzed qualitatively by optical analysis.

Table 5 (a) Resulting forces \bar{F} at reference conditions with $u_g = 2 \text{ m/s}$; (b) gas flow velocities u_g needed to achieve the reference conditions $\bar{F} = 1$; c resulting forces \bar{F} with $u_g = 3 \text{ m/s}$

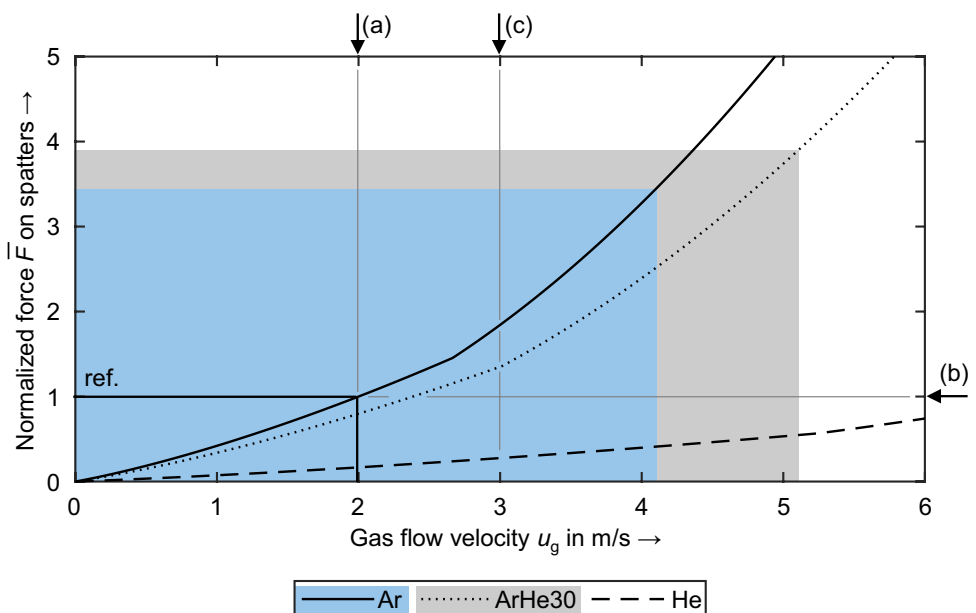
	(a)	(b)	(c)
	\bar{F} at $u_g = 2 \text{ m/s}$	u_g to achieve $\bar{F} = 1$ in m/s	\bar{F} at $u_g = 3 \text{ m/s}$
Ar	1.00	2.00	1.84
ArHe30	0.80	2.38	1.35
He	0.17	6.97	0.28

Afterwards, the spatters were collected and analyzed quantitatively. The methods are described in the following sections.

3.2.1 Optical analysis

Directly after the build job, the build platform cover was detached from the rope pull mechanism, extracted from the build chamber and placed into a photo box. A digital camera (PowerShot SX50 HS, Canon, Japan) was used to take pictures of the cover. For the evaluation and comparison between the gases, an analysis area of $270 \times 300 \text{ mm}^2$ was considered (see Fig. 5). As no spatters were found in front of the processed part in the negative x-direction, the analysis area was limited to the presented area in the positive x-direction. The analysis area was then further processed and turned into a binary image. In addition, a grid was added to enhance the comparability between the gases. The small black areas occurring directly above the processing zone were considered to be soot depositing on the plate and, thus, not further considered in the discussion.

Fig. 7 Normalized force \bar{F} exerted from a gas flow to a spatter depending on the gas flow velocity u_g ; the coloured rectangles denote the possible ranges of achievable forces \bar{F} up to the specific $u_{g,pu,min}$ for Ar (blue) and ArHe30 (gray); three cases are marked: **a** $u_g = 2 \text{ m/s}$, **b** $\bar{F} = 1$ and **c** $u_g = 3 \text{ m/s}$



3.2.2 Spatter analysis

Following the optical analysis, the spatters were characterized by their weight, size and shape. For this purpose, the spatters were sampled from the cover and weighed. Their PSD was then determined by dynamic image analysis according to ISO 13322-2 (Camsizer X2, Retsch, Germany), followed by an evaluation of the spatter shape by selective electron microscopy (SEM; JSM-IT200 InTouchScope, JEOL, Japan).

4 Results

4.1 Spatter transport

4.1.1 Particle pickup velocity for various gases

The resulting curves for the gas-dependent u_{pu} based on the model calculations presented in Sect. 2.2 are shown in Fig. 6. As can be seen, u_{pu} is the highest for small particle diameters for all gases (zone I). According to Eq. (5), zone I represents *Arch* numbers below 0.45. This is based on the comparably higher cohesive forces over the gravitational forces in this particle size regime. When the particle size increases over a certain size, u_{pu} decreases as the relation between cohesive force and gravitational force decreases (zone II). This decrease reaches a minimum within the constraints of this

study, after which the cohesive force becomes negligible compared to the gravitational force with a further increasing particle diameter. However, the gravitational force is still low compared to the cohesive force in this high particle size regime, which is why u_{pu} is generally lower at higher particle diameters (zone III).

The global minimum of these curves $u_{pu,min}$, which occurs at different particle diameters d_p for the various gases, represents the maximum applicable gas flow velocity $u_{g,max}$, which could theoretically be set in the machine per gas type. Above this velocity, powder particles from the powder bed with different diameters start to be blown away by the process gas flow. The resulting $u_{pu,min}$ for the various gases based on the model calculations are depicted with small circles in Fig. 6 and additionally summarized in Table 4. As shown in the table, Ar allows the lowest maximum gas flow velocity $u_{g,max}$ within the studied gases. With an increasing volume fraction of He in the process gas, the maximum gas flow velocity increases. Depending on the PSD of the powder material used, this maximum velocity could vary, which is exemplarily shown for the PSD of the 316L stainless steel powder used in the study (see the orange rectangle in Fig. 6). For this specific powder, $u_{g,max}$ for He deviates from the global minimum $u_{pu,min}$ for this gas–material combination. For Ar and ArHe30, however, $u_{g,max}$ coincides with $u_{pu,min}$, as the global minima lie within the used PSD.

Analyzing the calculation of u_{pu} in Sect. 2.2 reveals the main influencing gas property leading to the differences

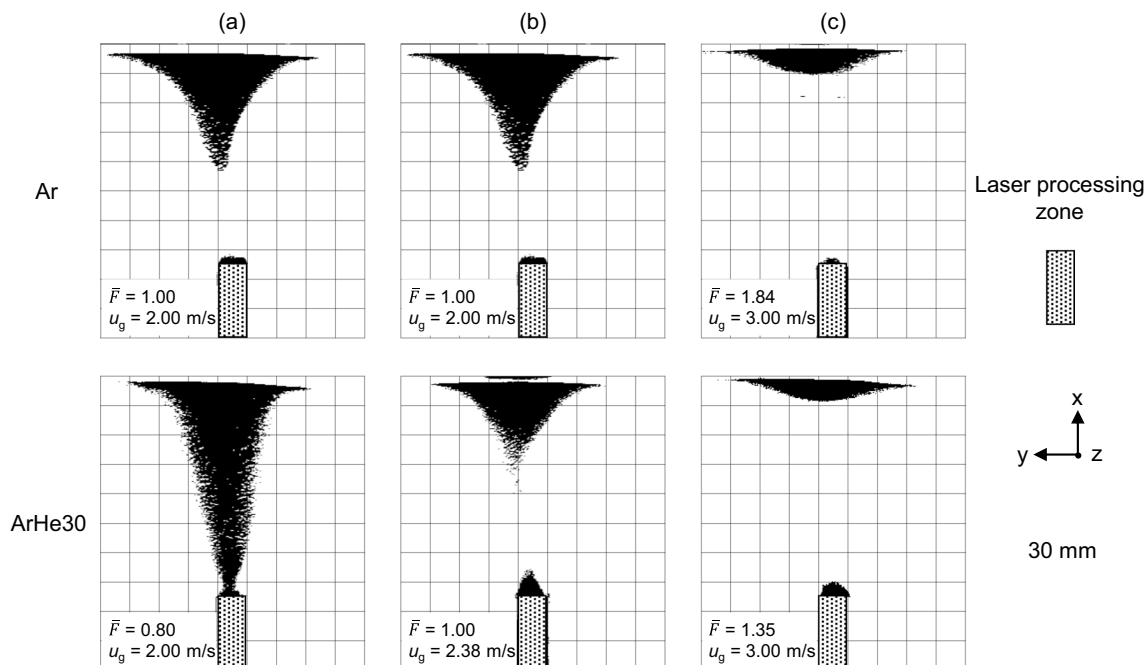
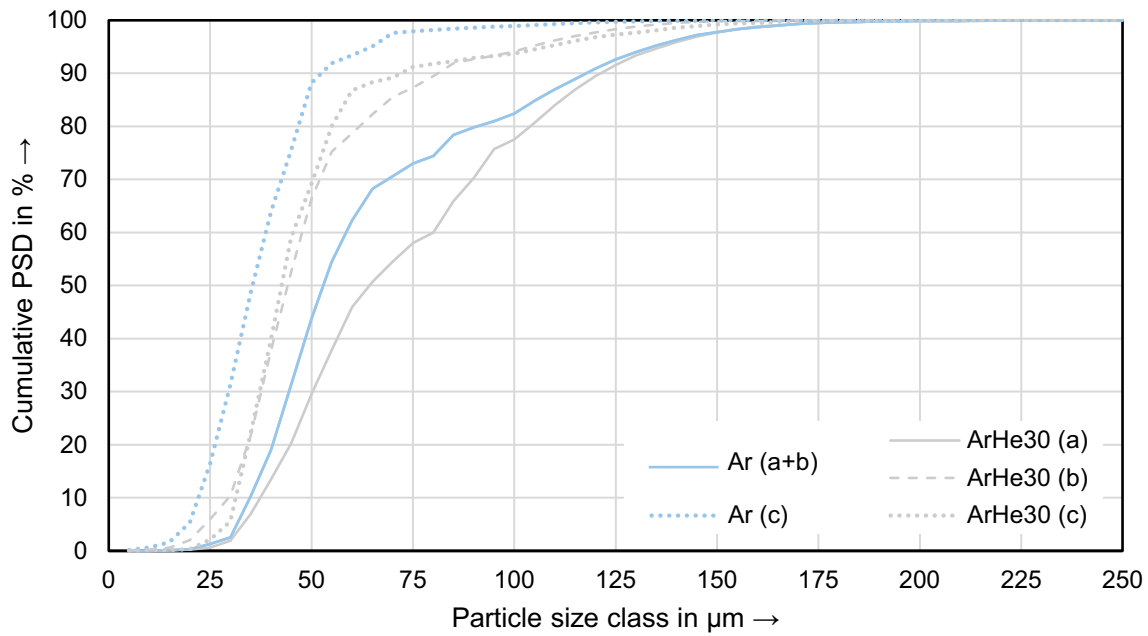


Fig. 8 Distribution of spatters on the powder bed; **a** similar gas flow velocity $u_g = 2$ m/s for both gases, **b** similar force on spatters $\bar{F} = 1$ for both gases, **c** similar gas flow velocity $u_g = 3$ m/s for both gases; Ref.: reference condition



		d_{10} in μm	d_{50} in μm	d_{90} in μm	Mass in g
(a)	Ar	34.9	53.1	117.5	7.91
	ArHe30	37.7	63.9	121.1	8.78
(b)	Ar	34.9	53.1	117.5	7.91
	ArHe30	29.6	43.8	80.1	3.18
(c)	Ar	22.6	35.8	51.9	1.53
	ArHe30	31.6	42.5	70.8	2.22

Fig. 9 Particle size distribution (PSD) and mass of collected spatters; **a** similar gas flow velocity $u_g=2$ m/s for both gases, **b** similar force on spatters $\bar{F} = 1$ for both gases, **c** similar gas flow velocity $u_g=3$ m/s for both gases

between the gases. For this, the dynamic viscosity η_g and the density ρ_g are used (see Eq. (4)). With a factor of approx. 9.95 between the densities and a factor of approx. 1.14 between the dynamic viscosities of both gases, the increased $u_{pu,min}$ of He leading to a higher $u_{g,max}$ compared to Ar can, thus, mainly be attributed to the lower ρ_g of He (see Table 1).

4.1.2 Force on spatters

The resulting normalized forces \bar{F} per gas depending on the gas flow velocity u_g are shown in Fig. 7. The reference condition $\bar{F}(\text{Ar}, u_g = 2\text{m/s}) = 1$ (ref.) is also depicted on the Ar curve in Fig. 7 by a black solid horizontal and vertical line. For better visibility, the maximum plotted gas flow velocity is $u_g = 6$ m/s. This includes $u_{pu,min}$ for the experimentally studied gases Ar and ArHe30 (see Table 4). In the comparison between the gases, three cases (a)–(c) are considered (highlighted with arrows in Fig. 7). Case (a) represents a build job with a gas flow velocity of $u_g = 2$ m/s. In case (b), a force of $\bar{F} = 1$ was applied on the spatters. Case (c) finally

exposes the potential influence of the gas flow, as the gas flow velocity was increased to $u_g = 3$ m/s. These three cases were also applied in the experiments. The blue and grey rectangles in Fig. 7 additionally visualize the potential of Ar and ArHe30 with respect to their maximum achievable force on spatters, as they are plotted considering the gas-dependent $u_{pu,min}$. To quantitatively compare the gases, Table 5 summarizes the resulting gas flow velocities and forces per gas. As Re_s reached a maximum value in the calculations of approx. 37 and 16 for Ar and He, respectively, the validity range given in Eq. (9) was complied with.

For the calculation of F , the gas density ρ_g and the gas flow velocity u_g are considered. As u_g contributes quadratically to F , this property plays a major role in compensating the lower ρ_g of He-containing gases compared to Ar. With similar gas flow velocities u_g , the removal of by-products is worse for He-containing gases compared to Ar (see Table 5(a) + (c)). However, by increasing u_g , F can be significantly increased to achieve a comparable removal of spatters as with Ar (see Table 5(b)). This is shown by the

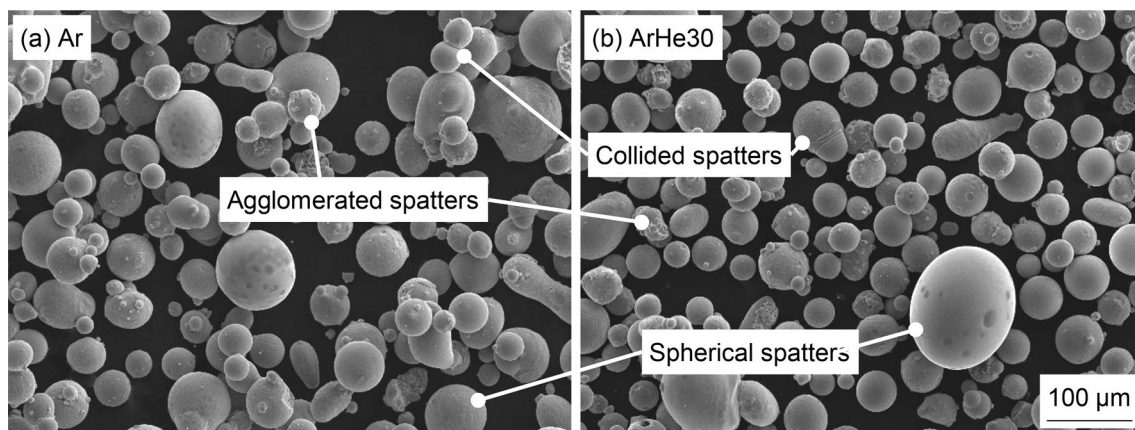


Fig. 10 SEM images of the collected spatters produced with $u_g = 2$ m/s under **a** Ar and **b** ArHe30; different types of spatters are highlighted

blue and grey rectangles in Fig. 7 highlighting the potential of He-containing gases. With ArHe30 and its higher $u_{g,max}$, for example, a higher maximum force F on spatters can theoretically be achieved compared to Ar.

4.2 Experimental investigations of the spatter removal

The theoretical considerations described in the previous Sect. 4.1 were applied to the PBF-LB/M process. Therefore, the process gases Ar and ArHe30 were studied with the three gas flow conditions (a)–(c) described in Table 5. Due to limitations of the PBF-LB/M machine used in the study, the respective particle pickup velocities for the gases $u_{pu,min}$ shown in Table 4 could not be reached (see Fig. 12 in the Appendix). However, to still highlight the potential of an increased gas flow velocity, $u_g = 3$ m/s was used as the maximum gas flow velocity in the experiments. First, the distribution of spatters over the powder bed is described in Sect. 4.2.1, followed by an analysis of the spatter characteristics in Sect. 4.2.2.

4.2.1 Distribution of spatters on the powder bed

Figure 8 shows the resulting distribution of spatters over the powder bed as collected by the experimental spatter collection setup for all three gas flow conditions (a)–(c). A qualitative analysis of Fig. 8 confirms the results from the theoretical considerations in Sect. 4.1. In the following discussion, the spread of the spatters along the x -axis and y -axis is considered as a measure to compare the gases. When the gas flow velocity was set to $u_g = 2$ m/s for all gases, Ar outperforms ArHe30 with regard to the removal of spatters (see Fig. 8a). The spatters spread further over the powder bed, both in the x - and y -direction, when using ArHe30. This

is related to the lower force \bar{F} that is applied to a spatter at this gas flow velocity $u_g = 2$ m/s. However, the possible range of gas flow velocities below the gas-dependent $u_{pu,min}$ enables the usage of gas flow velocities resulting in a comparable force on the spatters $\bar{F} = 1$ per gas (see Table 5(b)). In the PBF-LB/M process, this results in a reduced spread of spatters over the powder bed along the x - and y -directions for ArHe30 (see Fig. 8b). Additionally, a qualitatively reduced number of spatters accumulated for ArHe30 in case (b). When the gas flow velocity was finally increased to $u_g = 3$ m/s, the removal of spatters improved significantly for both gases. With this flow condition, most of the spatters were transported out of the analysis area with no significant differences between Ar and ArHe30.

4.2.2 Spatter characteristics

After comparing the spread of spatters over the powder bed, the spatters were collected and further characterized.

Figure 9 summarizes the results from the PSD measurements as well as from the weighing. First, the flow condition of a similar gas flow velocity $u_g = 2$ m/s for the two gases is compared (see Fig. 9a). The curve of the cumulative PSD of the ArHe30 spatters was slightly lower than that of the Ar spatters. For the ArHe30 process, about 0.9 g more spatters were collected. This result followed the comparison of these two processes in Fig. 8 (a), where more spatters were found to accumulate on the powder bed for ArHe30. Considering the PSD of these spatters, more large spatters were found under ArHe30. When the flow conditions applied second were compared, the results changed significantly (see Fig. 9b). The curve of the cumulative PSD of the ArHe30 spatters showed a shift toward smaller particle sizes compared to Ar, with a maximum difference of approx. 47% in the d_{90} value. Similarly, the mass of the collected spatters

for ArHe30 was found to be only 40% of that for Ar. These results from a flow condition with a similar removal of spatters based on the force F coincide with a positive effect of He-containing gases first reported by Pauzon et al. [13]. In their study, they found that fewer incandescent spatters were created in a He process compared to Ar. This was attributed to the comparably lower recoil pressure and, hence, a calmer melt pool with He. The third investigated flow condition of increased gas flow velocities (see Fig. 9c) showed comparable results to the first flow condition. A lower curve of the cumulative PSD as well as an increased weight of the collected spatters was found for the ArHe30 spatters. This was again correlated to the comparably higher force that Ar can apply to spatters and, thus, their improved removal. However, a significant decrease in the d_{90} values compared to the flow condition (a) could be identified. This shows the great potential of an increased gas flow velocity in terms of a higher process capability, as large spatters tend to settle closer to the processing zone and were reported in the literature to be particularly detrimental to the part properties [20, 33].

To compare the shape of the spatters, the sphericity determined by the dynamic image analysis as well as by scanning electron microscopes was investigated. Figure 10 shows SEM images of the spatters produced in the Ar and the ArHe30 processes at $u_g = 2$ m/s. Different types of spatters could be identified within both gases. Besides spherical spatters, agglomerated and collided spatters could be found and are highlighted in Fig. 10. This is in line with the classification of spatters proposed in the literature [4, 16, 21]. The sphericity measured by the optical analysis was found to be in a range from 70 to 100% for all gases with singular deviations to lower values for some gas flow conditions at specific particle size classes (see Fig. 13 in the appendix).

5 Conclusion

The presented study aimed at investigating the removal of spatters by various gases during the powder bed fusion of metals using a laser beam (PBF-LB/M). First, theoretical considerations were proposed to determine the potential of various gases to transport particles. To this end, the maximum gas flow velocity of a certain gas–material combination was calculated using the particle pickup velocity. This velocity describes the threshold above which the first particle of a certain size from a powder bed gets blown away. The potential of a gas flow to remove spatters from the processing zone can then be determined using the Stokes equation for the drag force. After these theoretical considerations, a unique experimental setup was applied to further investigate the removal of spatters. For the experiments, the 316 L stainless steel material was processed

with argon (Ar) and an argon–helium (Ar–He) mixture. The spread of the spatters over the powder bed as well as their characteristics were determined.

The main conclusions from this study are summarized as follows:

- Increasing the molar fraction of He in Ar increases the maximum applicable gas flow velocity in the PBF-LB/M process.
- Increasing the gas flow velocity can compensate for disadvantages of a lower gas density with regard to the removal of spatters.
- At an industry-standard gas flow velocity of 2 m/s, Ar can remove 316 L spatters away from the powder bed area better than an Ar–He mixture due to its higher density.
- A removal of 316 L spatters similar to that of Ar can be reached with Ar–He mixtures by increasing the gas flow velocity. In this comparison, a lower mass of spatters accumulated under the Ar–He mixture.
- When the gas flow velocity is increased to 3 m/s, nearly all 316 L spatters are removed from the powder bed area for Ar and Ar–He.

In future studies, the spatters should be divided by their shape and size according to their position on the powder bed to enhance the process understandings of PBF-LB/M. Additionally, the influence of the experimental setup on the fabrication of parts should be determined.

Appendix

See Figs. 11, 12 and 13.

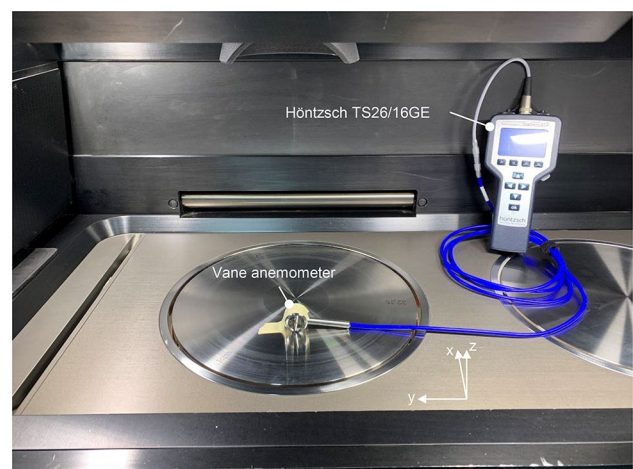


Fig. 11 Setup of the gas velocity measurements in the build chamber

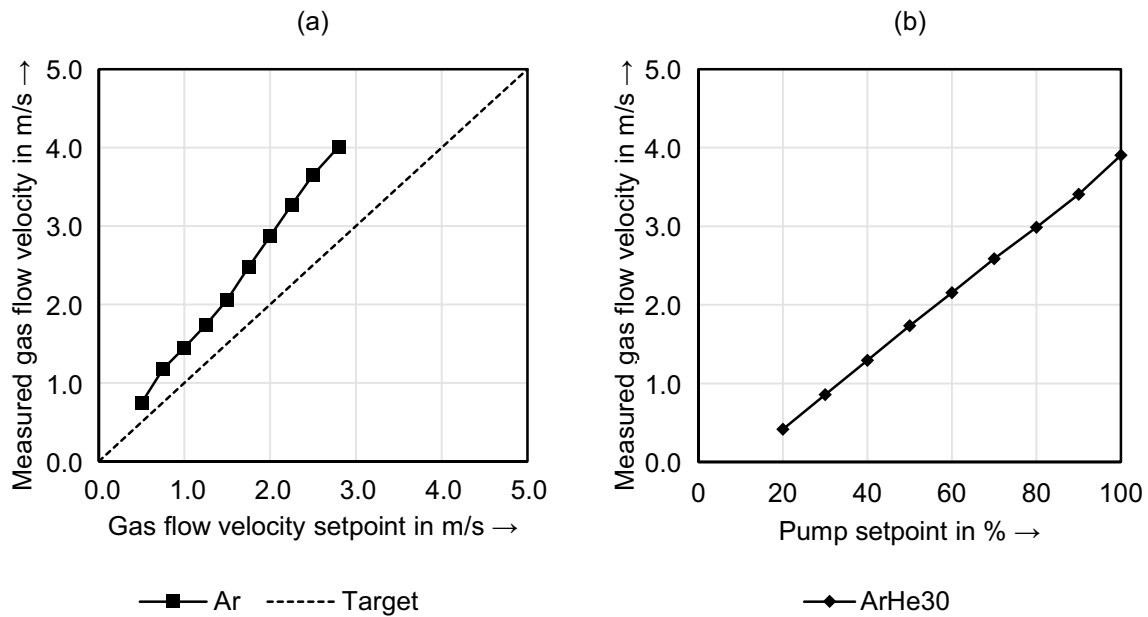
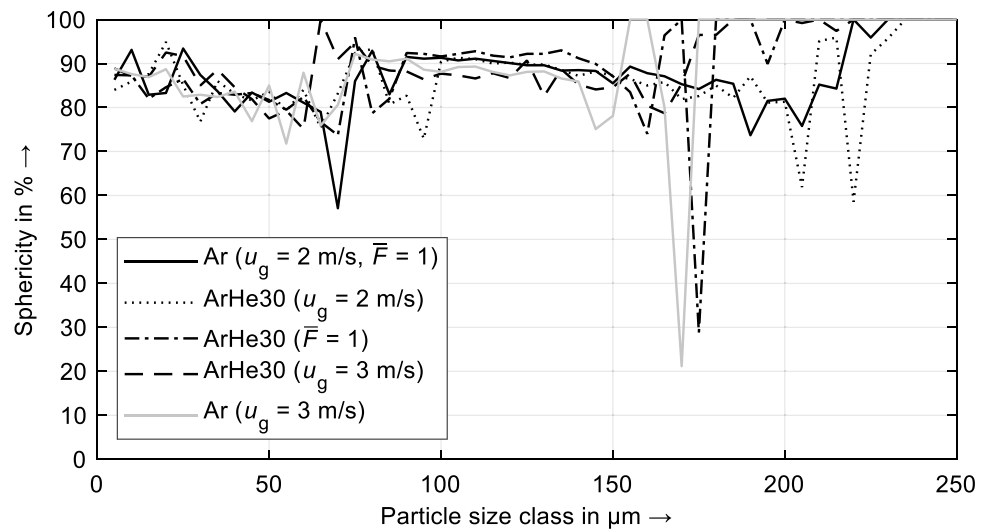


Fig. 12 Measured gas flow velocities: **a** Ar and **b** ArHe30

Fig. 13 Sphericity of spatters for Ar and ArHe30 at various gas flow conditions; u_g : gas flow velocity, \bar{F} : normalized force exerted from the gas flow on a single spatter



Funding Open Access funding enabled and organized by Projekt DEAL. Funding was provided by Bayerische Staatsministerium für Wirtschaft, Landesentwicklung und Energie (grant no. NW-1901-0013).

Declarations

Conflict of interest On behalf of all authors, the corresponding author states that there is no conflict of interest.

Open Access This article is licensed under a Creative Commons Attribution 4.0 International License, which permits use, sharing, adaptation, distribution and reproduction in any medium or format, as long as you give appropriate credit to the original author(s) and the source, provide a link to the Creative Commons licence, and indicate if changes were made. The images or other third party material in this article are included in the article's Creative Commons licence, unless indicated otherwise in a credit line to the material. If material is not included in the article's Creative Commons licence and your intended use is not permitted by statutory regulation or exceeds the permitted use, you will need to obtain permission directly from the copyright holder. To view a copy of this licence, visit <http://creativecommons.org/licenses/by/4.0/>.

References

- Gebhardt A (2016) Additive Fertigungsverfahren: Additive Manufacturing und 3D-Drucken für Prototyping—Tooling—Produktion, 5., neu bearbeitete und erweiterte Auflage. Hanser, Munich
- Chen H, Yan W (2020) Spattering and denudation in laser powder bed fusion process: multiphase flow modelling. *Acta Mater* 196:154–167. <https://doi.org/10.1016/j.actamat.2020.06.033>
- Santecchia E, Spigarelli S, Cabibbo M (2020) Material reuse in laser powder bed fusion: side effects of the laser—metal powder interaction. *Metals* 10:341. <https://doi.org/10.3390/met10030341>
- Li Z, Li H, Yin J et al (2022) A review of spatter in laser powder bed fusion additive manufacturing: in situ detection, generation, effects, and countermeasures. *Micromachines (Basel)* 13:1366. <https://doi.org/10.3390/mi13081366>
- Schniedenharn M, Wiedemann F, Schleifenbaum JH (2018) Visualization of the shielding gas flow in SLM machines by space-resolved thermal anemometry. *RPJ* 24:1296–1304. <https://doi.org/10.1108/RPJ-07-2017-0149>
- Ladewig A, Schlick G, Fisser M et al (2016) Influence of the shielding gas flow on the removal of process by-products in the selective laser melting process. *Addit Manuf* 10:1–9. <https://doi.org/10.1016/j.addma.2016.01.004>
- Slodczyk M, Ilin A, Kiedrowski T et al (2021) Spatter reduction by multi-beam illumination in laser powder-bed fusion. *Mater Des* 212:110206. <https://doi.org/10.1016/j.matdes.2021.110206>
- Zhang X, Cheng B, Tuffile C (2020) Simulation study of the spatter removal process and optimization design of gas flow system in laser powder bed fusion. *Addit Manuf* 32:101049. <https://doi.org/10.1016/j.addma.2020.101049>
- Keaveney S, Shmeliov A, Nicolosi V et al (2020) Investigation of process by-products during the selective laser melting of Ti6Al4V powder. *Addit Manuf* 36:101514. <https://doi.org/10.1016/j.addma.2020.101514>
- Heeling T, Gerstgrasser M, Wegener K (2017) Investigation of selective laser melting spatter characteristics for single- and multi-beam strategies using high speed imaging. In: *Lasers in manufacturing conference*, Munich, Germany
- Wimmer A, Zeller C, Bayerlein F et al (2018) Influence of the process gas on the laser beam melting process. In: *Proceedings of the 7th international conference on additive technologies*, Maribor, Slovenia, pp 66–70
- Bidare P, Bitharas I, Ward RM et al (2018) Fluid and particle dynamics in laser powder bed fusion. *Acta Mater* 142:107–120. <https://doi.org/10.1016/j.actamat.2017.09.051>
- Pauzon C, Hoppe B, Pichler T et al (2021) Reduction of incandescent spatter with helium addition to the process gas during laser powder bed fusion of Ti-6Al-4V. *CIRP J Manuf Sci Technol* 35:371–378. <https://doi.org/10.1016/j.cirpj.2021.07.004>
- Baehr S, Melzig L, Bauer D et al (2022) Investigations of process by-products by means of Schlieren imaging during the powder bed fusion of metals using a laser beam. *J Laser Appl* 34:42045. <https://doi.org/10.2351/7.0000808>
- Barrett C, Carradero C, Harris E et al (2019) Statistical analysis of spatter velocity with high-speed stereovision in laser powder bed fusion. *Prog Addit Manuf* 4:423–430. <https://doi.org/10.1007/s40964-019-00094-6>
- Young ZA, Guo Q, Parab ND et al (2020) Types of spatter and their features and formation mechanisms in laser powder bed fusion additive manufacturing process. *Addit Manuf* 36:101438. <https://doi.org/10.1016/j.addma.2020.101438>
- Guo Q, Zhao C, Escano LI et al (2018) Transient dynamics of powder spattering in laser powder bed fusion additive manufacturing process revealed by in-situ high-speed high-energy X-ray imaging. *Acta Mater* 151:169–180. <https://doi.org/10.1016/j.actamat.2018.03.036>
- Anwar AB, Pham Q-C (2018) Study of the spatter distribution on the powder bed during selective laser melting. *Addit Manuf* 22:86–97. <https://doi.org/10.1016/j.addma.2018.04.036>
- Lutter-Günther M, Bröker M, Mayer T et al (2018) Spatter formation during laser beam melting of AlSi10Mg and effects on powder quality. *Procedia CIRP* 74:33–38. <https://doi.org/10.1016/j.procir.2018.08.008>
- Wang D, Wu S, Fu F et al (2017) Mechanisms and characteristics of spatter generation in SLM processing and its effect on the properties. *Mater Des* 117:121–130. <https://doi.org/10.1016/j.matdes.2016.12.060>
- Obeidi MA, Mussatto A, Groarke R et al (2020) Comprehensive assessment of spatter material generated during selective laser melting of stainless steel. *Mater Today Commun* 25:101294. <https://doi.org/10.1016/j.mtcomm.2020.101294>
- Pauzon C, Hryha E, Forêt P et al (2019) Effect of argon and nitrogen atmospheres on the properties of stainless steel 316 L parts produced by laser-powder bed fusion. *Mater Des* 179:107873. <https://doi.org/10.1016/j.matdes.2019.107873>
- Pauzon C, Forêt P, Hryha E et al (2020) Argon-helium mixtures as laser-powder bed fusion atmospheres: towards increased build rate of Ti-6Al-4V. *J Mater Process Technol* 279:116555. <https://doi.org/10.1016/j.jmatprotec.2019.116555>
- Amano H, Ishimoto T, Sukanuma R et al (2021) Effect of a helium gas atmosphere on the mechanical properties of Ti-6Al-4V alloy built with laser powder bed fusion: a comparative study with argon gas. *Addit Manuf* 48:102444. <https://doi.org/10.1016/j.addma.2021.102444>
- Stokes MA, Khairallah SA, Volkov AN et al (2022) Fundamental physics effects of background gas species and pressure on vapor plume structure and spatter entrainment in laser melting. *Addit Manuf* 55:102819. <https://doi.org/10.1016/j.addma.2022.102819>
- Wilke CR (1950) A viscosity equation for gas mixtures. *J Chem Phys* 18:517–519. <https://doi.org/10.1063/1.1747673>
- Schudel W (1941) Über die Viskosität binärer Gasgemische. *Mitteilungen der Naturforschenden Gesellschaft Schaffhausen* 17:345–376. <https://doi.org/10.5169/SEALS-585521>
- Linde GmbH (2022) Internal database of gas properties
- Kalman H, Satran A, Meir D et al (2005) Pickup (critical) velocity of particles. *Powder Technol* 160:103–113. <https://doi.org/10.1016/j.powtec.2005.08.009>
- Springer-Verlag GmbH (2013) *VDI-Wärmeatlas*. Springer, Berlin
- Shen H, Rometsch P, Wu X et al (2020) Influence of gas flow speed on laser plume attenuation and powder bed particle pickup in laser powder bed fusion. *JOM* 72:1039–1051. <https://doi.org/10.1007/s11837-020-04020-y>
- Schiller L, Naumann A (1933) Über die grundlegende Berechnung bei der Schwerkraftaufbereitung. *Zeitschrift des Vereines Deutscher Ingenieure* 77:318–320
- Anwar AB, Ibrahim IH, Pham Q-C (2019) Spatter transport by inert gas flow in selective laser melting: a simulation study. *Powder Technol* 352:103–116. <https://doi.org/10.1016/j.powtec.2019.04.044>
- Ferrar B, Mullen L, Jones E et al (2012) Gas flow effects on selective laser melting (SLM) manufacturing performance. *J Mater Process Technol* 212:355–364. <https://doi.org/10.1016/j.jmatprotec.2011.09.020>

Publisher's Note Springer Nature remains neutral with regard to jurisdictional claims in published maps and institutional affiliations.